creative commons

COMMONS DEED

저작자표시-비영리-변경금지 2.0 대한민국

이용자는 아래의 조건을 따르는 경우에 한하여 자유롭게

- 이 저작물을 복제, 배포, 전송, 전시, 공연 및 방송할 수 있습니다.

다음과 같은 조건을 따라야 합니다:

저작자표시. 귀하는 원저작자를 표시하여야 합니다.

비영리. 귀하는 이 저작물을 영리 목적으로 이용할 수 없습니다.

변경금지. 귀하는 이 저작물을 개작, 변형 또는 가공할 수 없습니다.

- 귀하는, 이 저작물의 재이용이나 배포의 경우, 이 저작물에 적용된 이용허락조건을 명확하게 나타내어야 합니다.
- 저작권자로부터 별도의 허가를 받으면 이러한 조건들은 적용되지 않습니다.

저작권법에 따른 이용자의 권리는 위의 내용에 의하여 영향을 받지 않습니다.

이것은 이용허락규약(Legal Code)을 이해하기 쉽게 요약한 것입니다.

Disclaimer

dCollection

의학 박사 학위 논문

Intravoxel Incoherent Motion MRI-derived parameters and T2* relaxation time for noninvasive assessment of renal fibrosis

- an experimental study in a rabbit model of unilateral ureter obstruction -

복셀 내 화소 결집 운동 확산 강조 자기공명영상과 T2* 이완시간을 통한 신실질 섬유화의 비침습적 평가

- 일측성 요로폐쇄 토끼모델을 이용한 실험적 연구 -

2019년 2월

서울대학교 대학원

의과대학 의학과

우성민

Abstract

Introduction: The purpose of this study was to evaluate the association of apparent diffusion coefficient (ADC), intravoxel incoherent motion (IVIM) MRI-derived parameters, and T2* relaxation time with histopathological changes observed during renal fibrogenesis in a rabbit model of unilateral ureter obstruction (UUO)

Methods: This study was approved by the Animal Care and Use Committee of our institute (15-0274-C1A0). Twenty New Zealand White rabbits underwent baseline MRI followed by surgery (sham or UUO) and then follow-up MRI at postoperative day (POD) 0, 3, 7, and 14. MRI scans were acquired using a 3-Tesla system (Magnetom Trio, Siemens Medical Solutions, Erlangen, Germany) with a human knee coil. Hematoxylin and eosin and Masson's trichrome staining was performed to evaluate cell density and area of fibrosis. Spearman rank correlation and Pearson correlation tests and one-way analysis of variance were used for statistical analyses.

Results: There was a continuous increase in the area of fibrosis and cell density: rho = 0.900 (95% confidence interval [CI] = 0.760, 0.960; $p<0.0001$) and 0.904 (95% CI = 0.769, 0.962; $p<0.0001$), respectively. There was a tendency for all MRI variables to decrease at POD 3 and partly recover at POD 7. ADC, D, f, and T2* relaxation time showed significant correlation with area of fibrosis and cell density (r = -0.5177 and -

0.6962, -0.5395 and -0.7851, -0.7168 and -0.7902, and -0.6808 and -0.7212, respectively; p = 0.0052-0.0481) while D* did not (p = 0.1997 and 0.7853, respectively).

Conclusions: ADC, IVIM MRI-derived parameters, and T2* relaxation time were significantly associated with the area of fibrosis and cell density during renal fibrogenesis in a rabbit model of UUO. After validation in future studies, MRI may have potential for noninvasive assessment modality of renal fibrosis.

* This work has been published in *Magnetic Resonance Imaging*.

Woo S, Cho JY, Kim SY, Kim SH. Intravoxel incoherent motion MRI-derived parameters and T2* relaxation time for noninvasive assessment of renal fibrosis: An experimental study in a rabbit model of unilateral ureter obstruction. Magn Reson Imaging. 2018;51:104-112.

Keywords: chronic kidney disease, intravoxel incoherent motion, magnetic resonance imaging, renal fibrosis, T2*-weighted imaging, unilateral ureter obstruction

Student number: 2014-30638

Table of Contents

Abstract.....i

Contents.....iii

List of Tables.....iv

List of Figures.....v

Introduction.....1

Materials and Methods.....3

Results.....8

Discussion.....27

Bibliography.....34

초록 (국문).....40

List of Tables

Table 1. MRI Acquisition Parameters at 3.0-Tesla …….……..…...11

Table 2. Pairwise comparison of ADC, and IVIM-MRI, and T2*-weighted imaging parameters between four groups …..……...12

List of Figures

Figure 1. Unilateral ureter obstruction and sham operation methods….....13

Figure 2. Diagram shows experimental protocol and allocation of rabbits to four study groups……..……..…….....…14

Figure 3. Representative photograph showing slide scanned by Aperio ScanScope in order to obtain high quality micrographs……..…….15

Figure 4. Cell density assessment on hematoxylin and eosin-stained slides using Image J software…….…..….16

Figure 5. Area of fibrosis assessment on Masson's trichrome-stained slides using Image J software……..……..….18

Figure 6. Changes in fibrosis and cell density over time…….…….…20

Figure 7. Representative micrographs (original magnification, X200) of kidney with H&E staining and Masson's trichrome staining……..…..21

Figure 8. Representative axial MRI scans of right kidney at postoperative day 0, 3, 7, and 14 after sham or unilateral ureter obstruction operation……..23

Figure 9. Bar graphs showing change of MRI parameters over time during all time points excluding post-operative day

3……24

Figure 10. Correlation between area of fibrosis and MRI parameters.....25

Figure 11. Correlation between cell density and MRI parameters….....26

Introduction

The prevalence of chronic kidney disease (CKD), a progressive decrease in renal function, is steadily increasing and is being recognized as a major health problem [1]. The final common histopathological correlate of CKD is renal fibrosis [2]. Evaluation of the presence and degree of renal fibrosis is crucial as it may assess the severity of CKD and provide prognostic information (i.e., long-term renal function) [3; 4]. At present, renal biopsy is the only method that is accepted as the gold standard for diagnosing renal fibrosis. However, biopsy is not only prone to sampling error, as the retrieved specimen only represents a small portion of the kidney, it is also invasive in nature (i.e., post-biopsy hemorrhage) and therefore limits its use for frequent monitoring [5]. Therefore, there has been a clinically unmet need for a non-invasive technique to assess renal fibrosis.

Recently there has been remarkable advances in magnetic resonance imaging (MRI) technology. Especially, the apparent diffusion coefficient (ADC) derived from diffusion-weighted imaging (DWI) has shown promise as a non-invasive biomarker of renal fibrosis in clinical studies and in well-established animal models such as unilateral ureter obstruction (UUO) [6-8]. In murine and rat UUO models, in which one ureter is ligated and results in renal fibrosis approximately within one week, it has been shown that ADC values decrease over time possible reflecting the increased cell density (i.e., inflammatory cells and myofibroblasts) [7-9]. However, renal fibrosis is a multi-faceted process that includes changes in kidney structure (i.e., increased cell density), oxygenation (i.e. hypoxia), and hemodynamics (i.e., altered microcirculation) [10]; and novel MRI techniques need to be investigated for correlation with these phenomena.

Among them, intravoxel incoherent motion (IVIM) MRI and blood oxygen level-dependent (BOLD) MRI are two promising candidates. IVIM MRI, which uses biexponential fitting of DWI from multiple b-values, can be used to separately obtain information regarding "pure" diffusion characteristics and microcirculation- or perfusion-related characteristics [11; 12]. In addition, BOLD MRI can determine the intra-renal oxygen content, based on the fact that tissue content of paramagnetic deoxyhemoglobin is negatively associated with oxygen partial pressure of blood using T2* relaxation time or R2* (1/T2*) [13].

Therefore, the purpose of this study was to evaluate the association of ADC, IVIM MRI-derived parameters, and T2* relaxation time with histopathological changes observed during renal fibrogenesis in a rabbit model of UUO.

Materials and Methods

Unilateral Ureter Obstruction Model and Experimental Protocol

This study was approved by the Animal Care and Use Committee of our institute (15-0274-C1A0). A total of 20 male New Zealand White rabbits weighing 2.5-3.0 kg were used. In particular, rabbits were used for the purpose of this study for the following reasons: (1) Our team has had prior experience in various types of renal disease models using rabbits [14; 15]; (2) We speculated that the experimental process (i.e, surgical procedures) and the data analysis and interpretation would be more feasible when using rabbits due to their larger size compared with previous well-established animal models of UUO (i.e., murine or rat) [16].

UUO was performed according to previously described methods as shown in Figure 1 [7; 14]. Rabbits were first sedated with intravenous injection of 5 mg/kg of a tiletamine hydrochloride and zolazepam (Zoletil; Virbac, Carros, France) and 1-3 mg/kg of xylazine hydrochloride (Rompun; Bayer Korea, Seoul, Korea). After a midline abdominal incision was made, the proximal right ureter was gently exposed and ligated with nylon suture (4-0 Ethilon, Ethicon Inc., Somerville, NJ) at the proximal ureter followed by closure of the surgical wound. The experimental protocol for each rabbit consisted of a preoperative baseline MRI scan followed by surgery (UUO or sham operation) and then a postoperative follow-up MRI scan according to group allocation (Figure 2). The first group received only a “sham” operation (Figure 1), meaning that the rabbits underwent operation consisting of only midline incision followed by immediate closure of the surgical wound without performing a UUO procedure and then an

immediate follow-up MRI (day 0). This sham operation which did not involve ureteral obstruction of the kidney was performed on the basis that it would serve as a “control” for the other groups of rabbits in which UUO were performed on. On the other hand, the second to fourth groups underwent UUO followed by follow-up MRI at 3, 7, and 14 days, respectively, after surgery. After follow-up MRI, the rabbits were sacrificed using intravenous injection of 5 ml of potassium chloride under deep anesthesia per the methods described above, and the right kidney was harvested for histopathological examination.

MRI Scan

MRI scans were acquired using a 3-Tesla system (Magnetom Trio, Siemens Medical Solutions, Erlangen, Germany) with a human knee coil. After induction of anesthesia, as described above, all MRI scans were acquired in the prone position and included the whole right kidney. In order to minimize motion artifacts from respiratory movement, the abdomen was firmly bound with a thin strip of cloth. The MRI protocol consisted of axial T2-weighted fast spin echo, axial IVIM-MRI, and axial T2*-weighted gradient echo sequences. The detailed parameters are summarized in Table 1. Parametric maps for IVIM MRI-derived parameters (D, D*, f, and ADC) and T2* relaxation time were automatically obtained on a pixel-by-pixel basis using a prototype software program provided by the vendor (Siemens Healthcare, Erlangen, Germany). Specifically, ADC values were calculated based on a monoexponential fit using all available b-values (0, 50, 100, 200, 400, 800, and 1000 s/mm2). IVIM MRI-derived parameters were calculated according to the following equation using a non-linear biexponential fit [11]:

$$SI_b/SI_0 = (1-f) \times e^{-bD} + f \times e^{-bD*}$$

where SI_b and SI_0 are the mean signal intensities for b values of b and 0 s/mm^2, respectively, D is the true diffusion coefficient, D* is the pseudo-diffusion coefficient, and f is the perfusion fraction. T2* relaxation times were calculated by applying a monoexponential model using all available TE values (2.67, 7.50, 12.33, 17.16, 21.99, 26.82, and 31.65 msec). In order to reduce field inhomogeneity, a second-order shim correction was carried out over a local volume-of-interest ("shim box") encompassing the whole right kidney, prior to acquiring IVIM-MRI and T2*-weighted GRE sequences.

Image Analysis

Two radiologists, each with 6 years of experience in MRI and 19 years of post-fellowship experience in renal imaging independently performed image analysis blinded to information regarding group allocation of the rabbits. The ADC, IVIM MRI-derived parameters, and T2* relaxation time were measured in the right kidney at the interpolar area of the right kidney, which was selected on the basis that this was the area in which the greatest amount of parenchyma was visualized. For each kidney, five operator-defined region-of-interests (ROI)s, with approximately 20-40 pixels in size, were carefully placed in the renal parenchyma at approximately 45 degrees apart from one another, avoiding vessels and the renal sinus [7; 17]. Due to marked parenchymal thinning at the 7th and 14th postoperative MRI scans, ROIs could not be separately placed for the cortex and medulla, and therefore, each ROI as part of this study encompassed both the cortex and the medulla. ROIs were initially placed in the ADC map while referencing the T2-weighted images, and were transferred to the

corresponding parametric maps of IVIM MRI-derived parameters and T2* relaxation time at identical locations. The average value obtained from the five ROIs was determined representative of each kidney.

Histopathological Analysis

The harvested kidney specimens were sectioned in the transverse plane at the center of the kidney, similar to the plane of image acquisition of MRI, stained with hematoxylin and eosin (H&E) and Masson's trichrome (MT), and were scanned using Aperio ScanScope (Aperio, Vista, CA, USA) to obtain high quality micrographs (Figure 2). H&E staining and MT staining were performed to evaluate cell density and area of fibrosis, respectively. For assessment of cell density, five locations were carefully selected at a high power field (magnification of x 200) in a similar manner as for MRI measurements using ImageScope software (Aperio, Vista, CA, USA). Using the Image J software version 1.50i (http://rsb.info.nih.gov/ij) with the "threshold" and "analyze particle" plugins, cell density (x 10^3 cells/mm^2) was automatically calculated for each location as shown in Figure 3 [7]. The mean value of the five measurements was used as the representative value for each kidney. In order to quantify the area of fibrosis, the proportion of blue intensity on MT-stained slides was calculated using the "threshold" plugin on Image J software (Figure 4). Hue of 121-179, saturation of 20-255, and intensity of 10-255 was defined as "blue intensity as used in the previous studies that have quantified the degree of fibrosis [18; 19].

Statistical Analysis

The Spearman rank correlation coefficient (rho) was used to evaluate the changes in histopathological findings (area of fibrosis and cell density) and MRI findings over time. For comparison of the MRI parameters between the four groups, one-way analysis of variance was used with post-hoc Tukey's honestly significant difference (HSD) test. The Pearson correlation coefficient (r) was used to assess the relationship between histopathology and MRI parameters. Only the data from POD 0, POD 7, and POD 14 were used for the purpose of assessing the relationship between histopathological and MRI parameters, as preliminary analysis demonstrated a marked deviation in the signal intensity on all MRI sequences in POD 3 group, speculated to be associated with marked venous congestion on histological specimens. Intra-class correlation (ICC) coefficients were used to assess inter-observer agreement. The degree of agreement was categorized as the following: ICC <0.4, poor; 0.4-0.75, fair; and >0.75, excellent [20].

A two-sided p value of <0.05 was considered statistically significant except for the post-hoc HSD test in which multiple comparisons (six comparisons between four groups) were performed and a Bonferroni-corrected p value of <0.008 (= 0.05/6) was used. Statistical analyses were performed using SPSS version 21 (IBM, Armonk, NY, USA) and MedCalc version 14.8.1 (MedCalc Software, Ostend, Belgium).

Results

Changes in Fibrosis and Cell Density over Time

The progressive changes in fibrosis and cell density from POD 0 though POD 14 are shown in Figure 6 and their corresponding representative micrographs of each group are presented in Figure 7. There was a continuous increase in both the area of fibrosis and cell density: rho = 0.900 (95% confidence interval [CI] = 0.760, 0.960; p <0.0001) and rho = 0.904 (95% CI = 0.769, 0.962; p <0.0001), respectively.

Comparison of MRI Parameters between Four Groups

The pairwise comparisons between ADC, IVIM-MRI, and T2*-weighted imaging parameters between the four groups are presented in Table 2 and their corresponding representative MRI scans are shown in Figure 8. After the UUO procedure, ADC and D significantly decreased at POD 3 compared with POD 0 (p <0.0001 for both) and then significantly increased at POD 7 compared with POD 3 (p = 0.0025 and 0.0032, respectively). ADC and D did not show significant difference from POD 7 to POD 14 (p = 0.6014 and 0.3231, respectively). Perfusion-related parameters of D* and f also showed a significant decrease at POD 3 compared with POD 0 (p = 0.0017 and 0.0001, respectively). Their mean values slightly increased from POD 3 to POD 7, although it was not statistically significant (p = 0.0838 and 0.3129, respectively). D* and f did not show significant difference from POD 7 to POD 14 (p = 0.6080 and 0.5107, respectively). T2* relaxation time significantly decreased from POD 0 to POD 3 (p = 0.0081). However, no significant differences were seen between POD 3 and POD 7 (p = 0.7330)

and between POD 7 and POD 14 (p = 0.3728). When excluding data from POD 3, due to aforementioned reasons, there was a continuous decrease in all MRI parameters except for D* over time (Figure 9): ADC (rho = -0.661 [95% CI = -0.877, -0.226; p = 0.0072]), D (rho = -0.805 [95% CI = -0.933, -0.497; p = 0.0003]), f (rho = -0.794 [95% CI = -0.929, -0.476; p = 0.0004], and T2* relaxation time (rho = -0.756 [95% CI = -0.914, -0.398; p = 0.0011]. D* did not show a significant trend (rho = -0.0758 [95% CI = -0.566, 0.454; p = 0.7883]).

Correlation between Histopathology and MRI Parameters

The correlation between histopathological findings (area of fibrosis and cell density) and MRI parameters (ADC, D, D*, f, and T2* relaxation time) are graphically presented in Figure 10 and 11, respectively. All MRI variables except for D* showed a significant negative correlation with area of fibrosis: ADC (r = -0.5177 [95% CI = -0.8141, -0.0074]; p = 0.0481), D (r = -0.5395 [95% CI = -0.8240, -0.0376]; p = 0.0379), f (r = -0.7168 [95% CI = -0.8990, -0.3231]; p = 0.0026), and T2* relaxation time (r = -0.6808 [95% CI = -0.8846, -0.2588]; p = 0.0052). However, D* did not demonstrate a significant correlation with the area of fibrosis (p = 0.1997). Similarly, all MRI variables other than D* was significantly and negatively correlated with cell density: ADC (r = -0.6962 [95% CI = -0.8908, -0.2860]; p = 0.0039), D (r = -0.7851 [95% CI = -0.9253, -0.4565]; p = 0.0005), f (r = -0.7902 [95% CI = -0.9272, -0.4669]; p = 0.0005), and T2* relaxation time (r = -0.7212 [95% CI = -0.9007, -0.3314]; p = 0.0024). In contrast, D* was not significantly correlated with cell density (p = 0.7853).

Inter-reader Agreement of MRI Parameters

The ICC coefficients were 0.969 (95% CI = 0.9235, 0.9876) for ADC, 0.9178 (95% CI = 0.8046, 0.9666) for D, 0.5897 (95% CI = 0.2106, 0.8146) for D*, 0.9579 (95% CI = 0.8970, 0.9831) for f, and 0.8995 (95% CI = 0.7642, 0.9590) for T2* relaxation time. Therefore, inter-reader agreement was considered excellent for ADC, D, f, and T2* relaxation time. However, D* was considered to demonstrate only moderate agreement.

Table 1. MRI Acquisition Parameters at 3.0-Tesla

Sequence	T2-weighted TSE	FS DW SSSE EPI	T2*-weighted GRE
TR/TE(msec)	4000/101	2300/79	100/2.67, 7.50, 12.33, 17.16, 21.99, 26.82, 31.65
FA (º)	180	180	45
Matrix	256 x 172	128 x 128	128 x 128
FOV (mm x mm)	120 x 80	120 x 120	120 x 120
ST (mm)	3	3	3
NEX	3	9	4
B-values (s/mm^2)		0, 50, 100, 200, 400, 800, 1000	
Acquisition time	2min 30sec	6min 45sec	2min 59sec

DW = diffusion-weighted; EPI = echo planar imaging; FA = flip angle; FOV = field of view; FS = fat-suppression; GRE = gradient echo; SSSE = single shot spin-echo; NEX = number of excitations; ST = slice thickness; TR/TE = relaxation time/echo time; TSE = turbo spin-echo

Table 2. Pairwise comparison of ADC, and IVIM-MRI, and T2*-weighted imaging parameters between four groups

Parameter/ POD	Measurement	P value*		
		3 days	7 days	14 days
ADC (x 10^{-3} mm^2/sec)				
0 days	1.41 (1.28; 1.54)	<0.0001†	0.1748	0.0165
3 days	1.03 (0.97; 1.10)		0.0025†	0.0311
7 days	1.28 (1.19; 1.38)			0.6014
14 days	1.21 (1.07; 1.35)			
D (x 10^{-3} mm^2/sec)				
0 days	1.38 (1.25; 1.50)	<0.0001†	0.0778	0.0023†
3 days	1.00 (0.93; 1.08)		0.0032†	0.1041
7 days	1.23 (1.10; 1.36)			0.3231
14 days	1.14 (1.04; 1.23)			
D* (x 10^{-3} mm^2/sec)				
0 days	29.20 (26.31; 32.09)	0.0017†	0.2424	0.8890
3 days	23.36 (20.87; 25.85)		0.0838	0.0072†
7 days	26.68 (23.94; 29.42)			0.6080
14 days	28.28 (26.45; 30.11)			
f (%)				
0 days	19.76 (17.21; 22.31)	0.0001†	0.0027†	0.0002†
3 days	9.80 (5.96; 13.64)		0.3129	0.9806
7 days	12.72 (8.49; 16.96)			0.5107
14 days	10.42 (9.10; 11.74)			
$T2^*$ relaxation time (msec)				
0 days	26.96 (23.14; 30.78)	0.0081†	0.0624	0.0022†
3 days	17.16 (13.08; 21.24)		0.7330	0.9201
7 days	19.84 (12.21; 27.47)			0.3728
14 days	15.52 (11.74; 19.30)			

Note. – Data are medians. Data in parentheses are ranges.

ADC = apparent diffusion coefficient; D = diffusion coefficient; D* = pseudo-diffusion coefficient; f = perfusion fraction; POD = postoperative day

*P values obtained from one-way ANOVA followed by post-hoc Tukey's honestly significant difference test.

†Significant with Bonferroni-corrected p value of <0.0083.

Figure 1. Unilateral ureter obstruction (UUO) and sham operation methods. After anesthesia, midline incision, and exposure of right ureter, UUO was done (left), followed by closure of abdomen. For sham operation, all procedures were done except for UUO itself in order to serve as control.

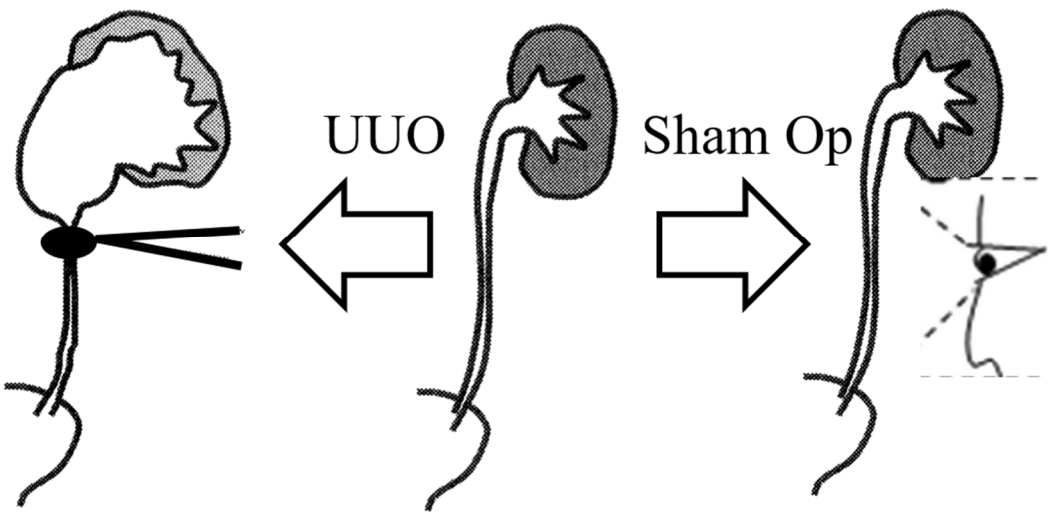

Figure 2. Diagram shows experimental protocol and allocation of rabbits to four study groups. Five rabbits in each group underwent (1) preoperative MRI, (2) operation, (3) postoperative follow-up MRI (at 0, 3, 7, and 14 postoperative day), followed by (4) histopathological examination. Group 1 underwent sham operation whereas groups 2-4 underwent unilateral ureter obstruction (UUO) procedure.

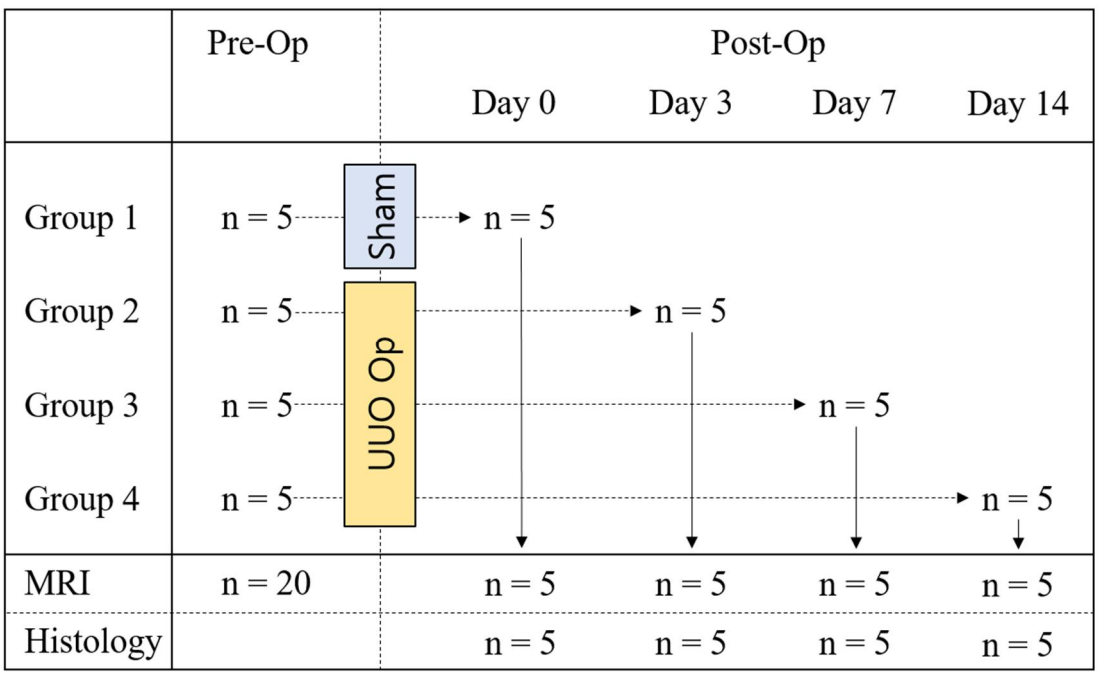

Figure 3. Representative photograph showing slide scanned by Aperio ScanScope in order to obtain high quality micrographs.

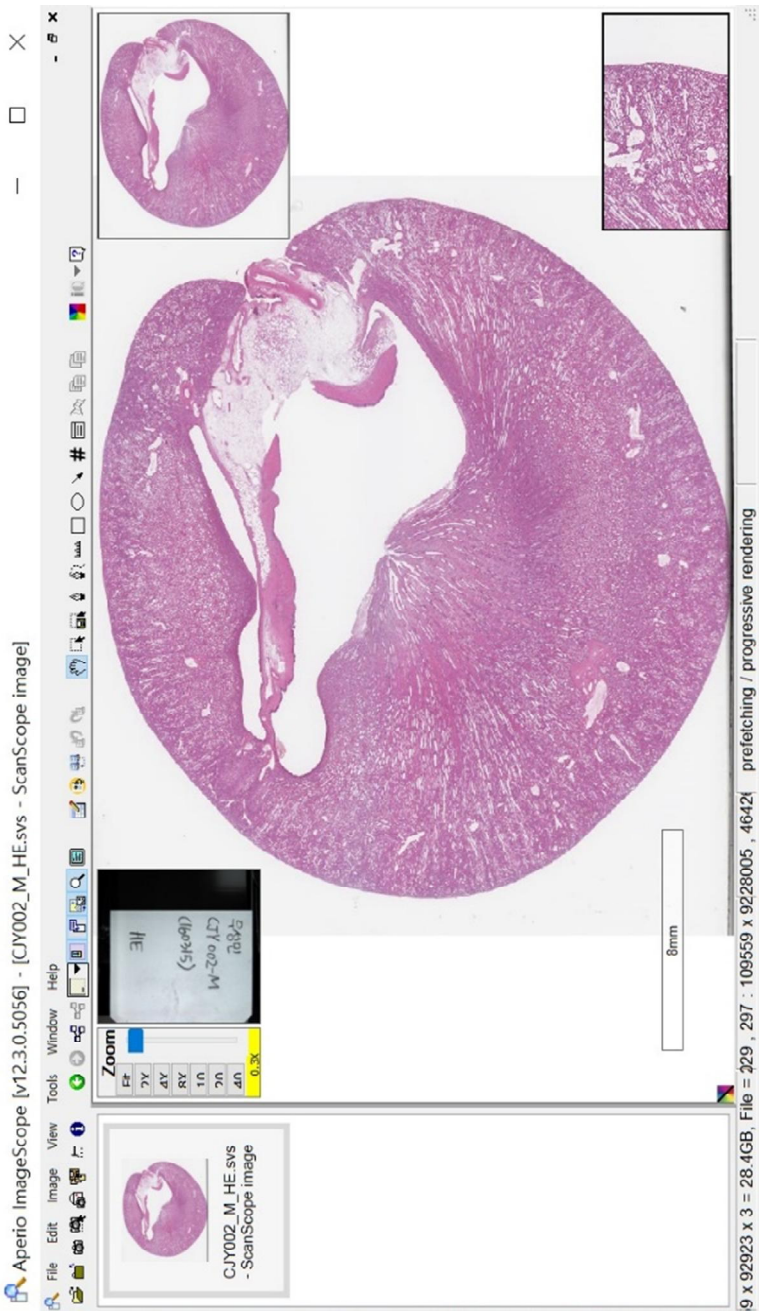

Figure 4. Cell density assessment on hematoxylin and eosin (H&E)-stained slides using Image J software.

A)

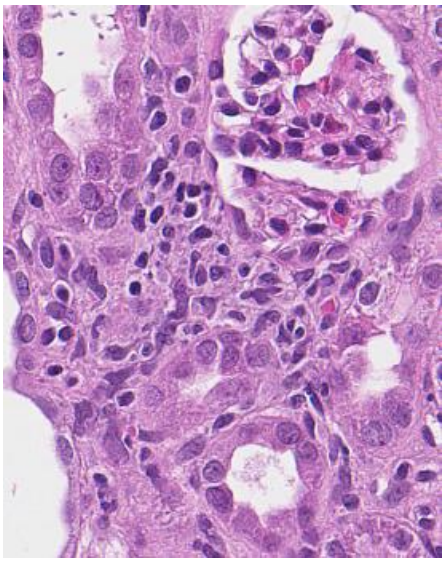

B)

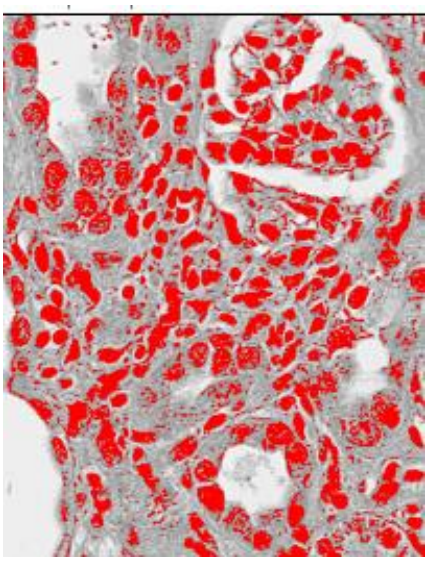

C)

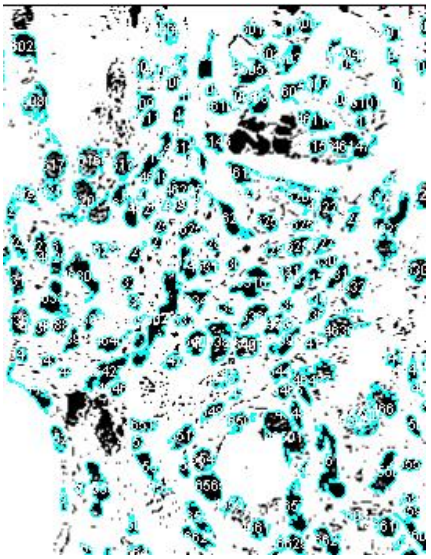

Figure 4. *(continued)*

A) H&E staining showing representative micrograph of rabbit kidney.

B) Nuclei, as surrogate of cells, were detected using "threshold" plug-in in Image J.

C) Cell number was counted using "analyze particle" plug-in in Image J, and in turn divided by area for determination of cell density (x 10^3 cells/mm^2)

points **Figure 9.** Bar graphs showing change of MRI parameters over time during all time points excluding post-operative day 3. ADC, D, f and T2* relaxation time showed a continuous decrease over time (rho = -0.661 to -0.805, p = 0.0003-0.0072). However, D* did not show a particular trend over time (p = 0.7853).

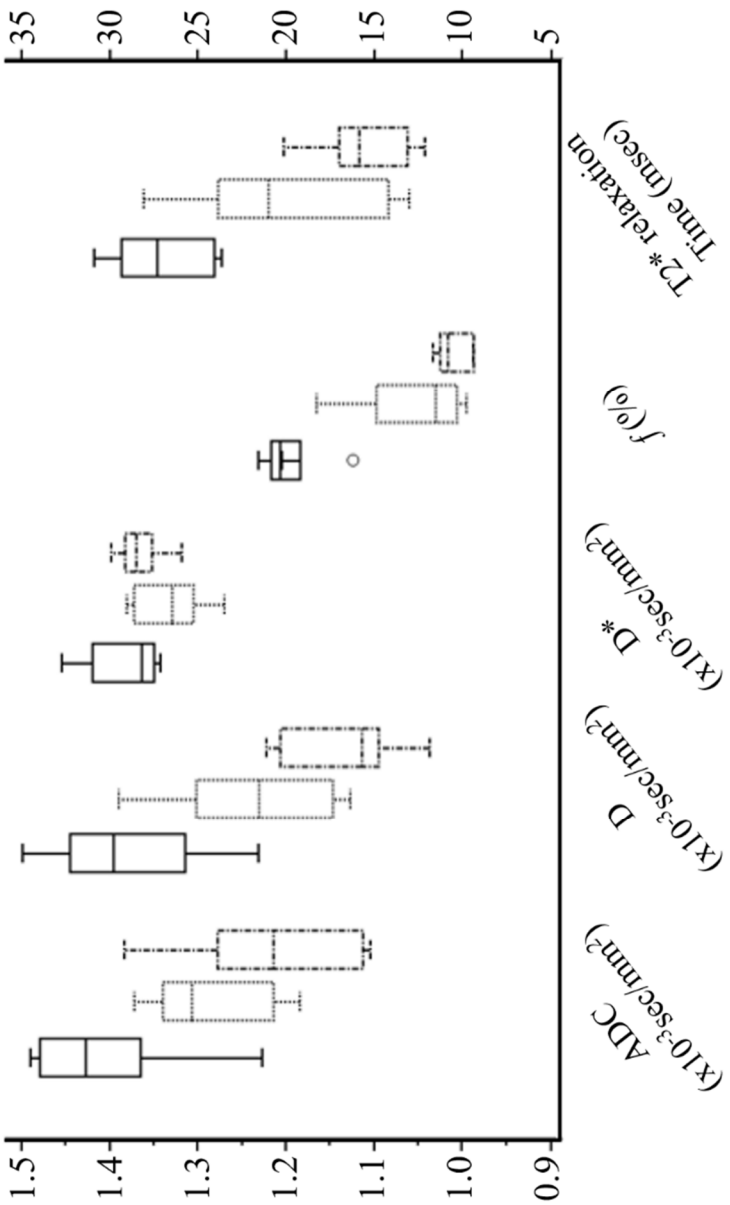

Figure 10. Correlation between area of fibrosis and MRI parameters. ADC, D, *f* and T2* relaxation time showed a significant negative correlation with degree of fibrosis (p = 0.0052-0.0481). However, D* did not demonstrate a significant correlation with the degree of fibrosis (p = 0.1997).

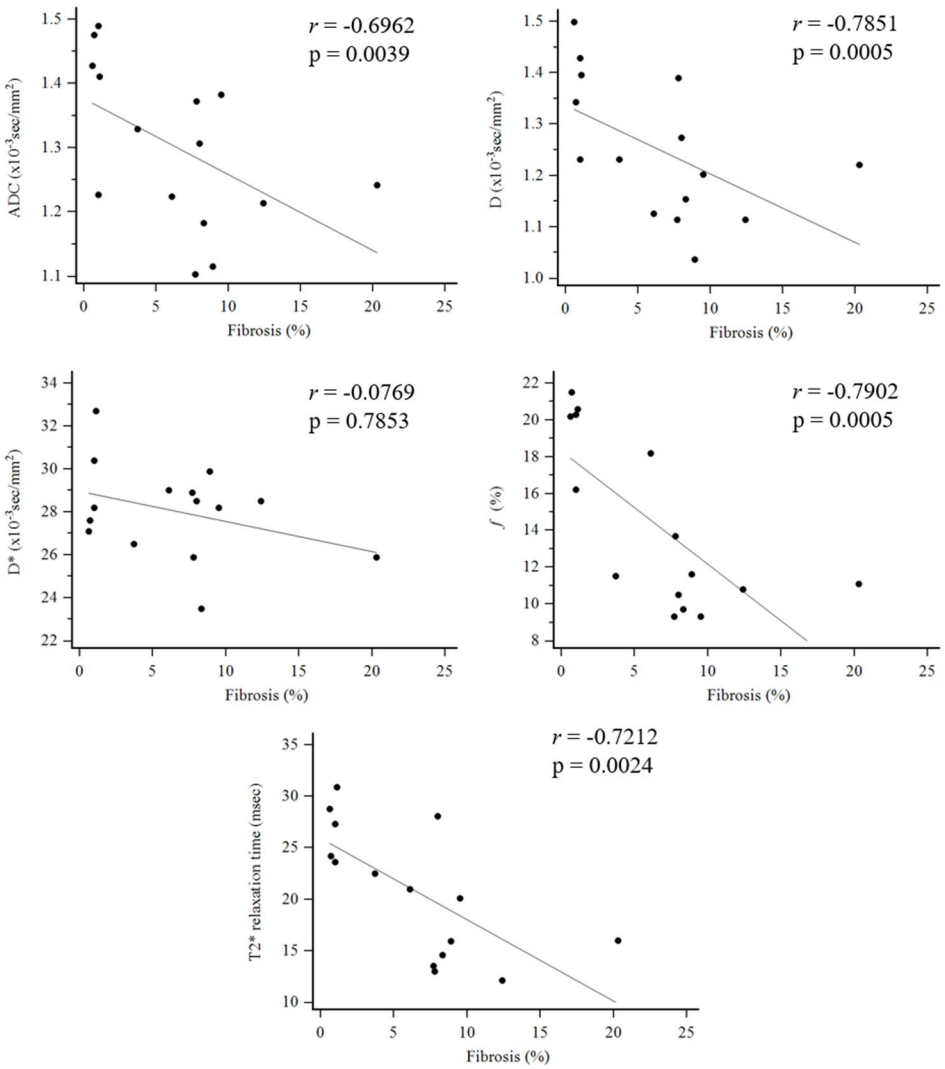

Figure 11. Correlation between cell density and MRI parameters. ADC, D, f and T2* relaxation time showed a significant negative correlation with cell density (p = 0.0005-0.0039). However, D* was not significantly correlated with cell density (p = 0.7853).

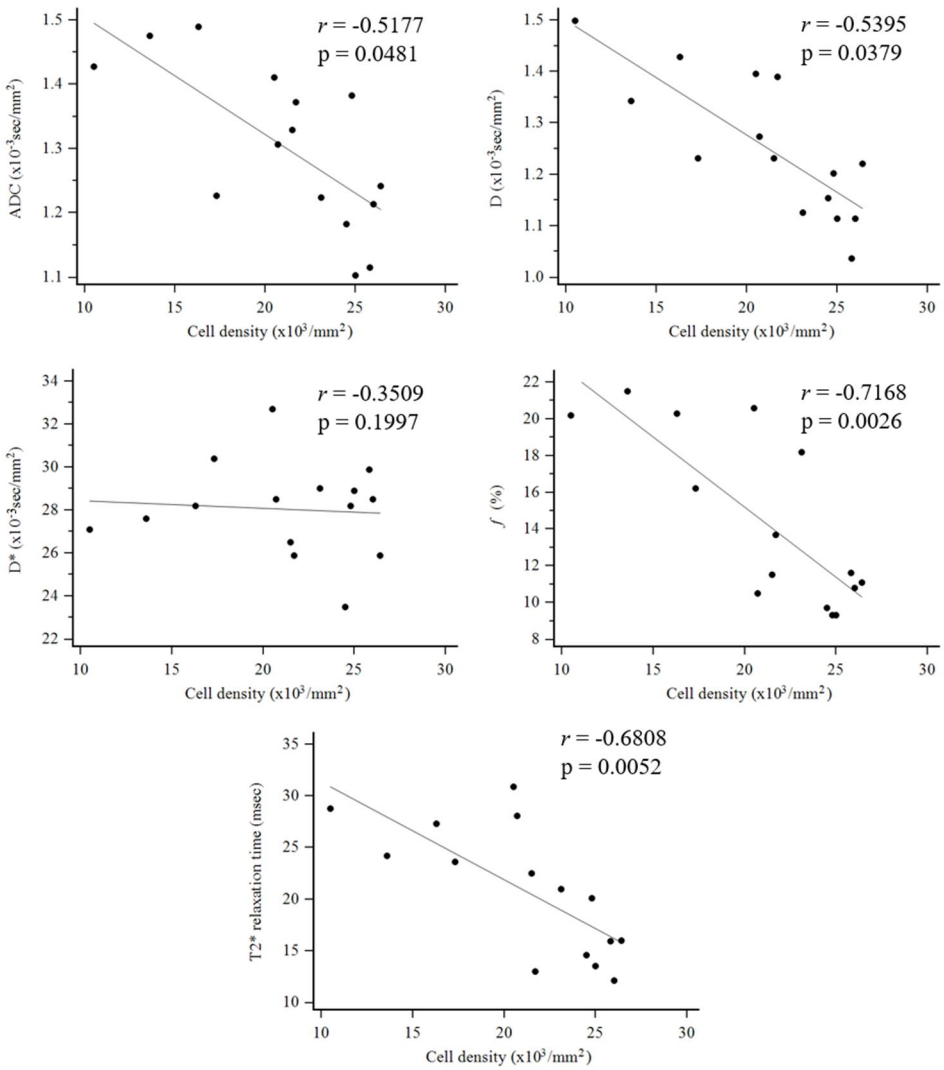

Discussion

In our study, we aimed to evaluate the association of ADC, IVIM MRI-derived parameters, and T2* relaxation time with histopathological changes observed during renal fibrogenesis in a rabbit model of UUO. After the UUO procedure we observed a continuous increase in both the area of fibrosis and cell density. All MRI parameters except for D* (ADC, D, f, and T2* relaxation time) demonstrated a significant negative correlation with both the area of fibrosis and cell density. There has been scattered reports showing potential for various MRI techniques in human clinical studies and animal models of UUO in mice or rats [7; 21; 22]. However, to the best of our knowledge, this is the first study to demonstrate the potential value of ADC, IVIM MRI-derived parameters and T2* relaxation time in a rabbit model of UUO. The results of our study generally corroborate the findings in the previous literature. With further validation of these various MRI sequences, and using a multiparametric approach may allow MRI to be a potential candidate for noninvasive assessment modality of renal fibrosis.

Since the study by Togao et al [7], in which the investigators observed that ADC values decreased during the progression of renal fibrosis induced by UUO in a murine model, it has been well accepted that ADC may serve as a useful biomarker of renal fibrosis. Togao et al [7] suggested that the decrease in ADC was attributed to the increased cell density. Increased cell density restricts the Brownian motion of waters molecules, leading to “diffusion restriction” [23]. In fact, one of the important changes seen during renal fibrogenesis is inflammatory cell and myofibroblast infiltration [24]. However, compared with ADC derived from monoexponential fitting of data acquired from DWI, a more advanced MRI technique, IVIM MRI, which uses biexponential

fitting of DWI from multiple b-values, can provide additional information. IVIM MRI is able to separate "pure" diffusion-related (i.e., "D") and microcirculation- or perfusion-related characteristics (i.e., "D*" and "f") [11; 12]. In our study, not only was ADC inversely correlated with the area of fibrosis (r = -0.5177) and cell density (r = -0.6962), but D also showed a stronger degree of inverse correlation, especially regarding cell density (r = -0.5395 and r = -0.7851 for area of fibrosis and cell density, respectively). It may be suggested that D may show potentially higher correlation with cellularity as it theoretically is without the mixed perfusion-related contribution included in ADC. Similar phenomena, that is better correlation with cell density using D than ADC, have been observed in the studies assessing cellularity in other organs (i.e., hepatocellular carcinomas and gliomas) [25; 26].

Using IVIM MRI allowed us to further explore the perfusion-related changes by using parameters of f and D*. This may have important clinical implications as hemodynamic changes are seen during the progression of renal fibrogenesis such as a decrease in the post-glomerular peritubular capillary blood flow and alteration of vascular endothelial growth factor [27; 28]. In our study, we found that f was significantly and inversely correlated with the area of fibrosis (r = -0.7902, p =0.0005) whereas D* did not show a significant relationship (r = -0.0769, p = 0.7853). In a previous study of rat UUO model by Cai et al [22], both f and D* were shown to be inversely correlated with area of fibrosis. Especially, f demonstrated changes at an earlier time-point than did D* and was considered more sensitive. In addition, both f and D* were significantly correlated with histopathological fibrosis in a recent human study [29]. On the contrary, in another human study, Ichikawa et al [30] observed that while D* was

lower in patients with lower renal function in terms of lower glomerular filtration rate, f did not show any significant difference. Therefore, it seems that perfusion-related information from IVIM MRI could be associated with the progression of renal fibrogenesis, but it is not robust enough to be used as of now. We speculate that several factors may have attributed to the discrepancies between studies. First, although IVIM MRI was used, there were differences in the number and choice of b-values. As signal intensity measurements at low b-values (≤100 s/mm^2) are more sensitive to noise, biexponential fitting has been shown to be less consistent for D* and f than ADC and D (coefficient of variation = 13.4-21.6% vs 7.9-8.1%, respectively) in the human liver [12; 25]. However, test-retest measurements specific for the current rabbit model was not done. Although similar trends will be expected, exact knowledge of the reproducibility of the IVIM MRI-related parameters and T2* relaxation time will be needed. Second, in terms of inter-observer agreement, a similar trend for poorer agreement using D* was also demonstrated in our study, with an intra-class correlation coefficient of 0.5897, signifying only moderate agreement, compared with that of other MRI variables (0.8995-0.9690), which showed excellent agreement. Third, the difference in subjects, that is whether IVIM MRI was performed in rabbits, rats, or humans, may have affected the results. Fourth, although IVIM modeling aims to separate diffusion- and perfusion-related characteristics of diffusion-weighted imaging, D* and f may only theoretically calculate perfusion-related information. Based on several well-known hypotheses, D* is more representative of the velocity of blood flow, while f is speculated to represent fractional volume of capillaries [31; 32]. Fifth, it has also been suggested that perfusion related information can be significantly affected by TE (which was different between our

and previous studies) due to relaxation differences. This can be overcome by methods such as simultaneous estimation of tissue T2 relaxation times and acquiring compensated perfusion fraction in the IVIM model [33].

In our study, we found that T2* relaxation time also was significantly associated with the area of fibrosis ($r = -0.7212$, $p = 0.0024$) and cell density ($r = -0.6808$, $p = 0.0052$) and showed similar temporal changes with ADC, D and f parameters. The proportion of oxyhemoglobin and deoxyhemoglobin, which is correlated with partial oxygen pressure in the blood, which is considered to be in equilibrium with surrounding tissue, affects T2* relaxation time—therefore enabling BOLD MRI to assess hypoxia [13]. Hypoxia is one of the key components in the pathophysiology of CKD and our study results show that T2* relaxation time could potentially be surrogate marker [34]. Previous studies have also shown similar correlation between T2*-weighted imaging parameters (T2* relaxation time or R2*) and renal pathology. Inoue et al [35] reported that T2* relaxation time was significantly inversely correlated with glomerular filtration rate in CKD patients ($r = -0.23$, $p < 0.01$). In addition, it was shown that R2* was sensitive for evaluating the progressive changes of hypoxia in a diabetic mouse model [36].

Some limitations of our study warrant mention. First, the number of study subjects were relatively small. This could have been partially overcome by performing follow-up MRI for all the intended periods (eg, obtaining follow-up MRI at POD 0, 3, 7, and 14 for the POD 14 group). Second, we were unable to separately analyze the cortex and medulla as the marked thinning of the parenchyma, especially at the 7th and 14th PODs, limited us from differentiating the anatomical layers. This may have been

associated with differential responses to ureter obstruction between various animal models, and technical factors such as the magnetic field strength and acquisition parameters. Previous studies using UUO model in mice analyzed the whole renal parenchyma without differentiating the cortex and medulla similarly to our study [21] or only the cortex [7] while another study using UUO model in rats provided separate results for the cortex, inter medulla, and outer medulla [22]. In the latter, a similar relationship between MRI and histopathological characteristics was seen for each of the anatomical segments, suggesting that either analyzing them separately, or as a whole, would have produced similar results [22]. Using renal fibrosis models with methods other than UUO, such as renal ischemia-reperfusion injury, subtotal nephrectomy, nephrotoxic serum nephritis, or Adriamycin-induced nephropathy, may overcome this limitation as they do not result in marked thinning of the parenchyma [37]. Other methods, such as partial UUO, rather than complete UUO performed in our study, could be an alternative. However, inducing similar degrees of partial obstruction for each animal subject would be difficult. In addition, it would be expected to take longer to achieve a similar degree of renal fibrosis and may cause pain to the animal subject for unnecessarily prolonged periods. Third, we acquired MRI scans in the axial plane and only evaluated the right kidney in which UUO procedure was performed due to technical reasons regarding MRI (i.e., acquisition time, signal-to-noise-ratio, and voxel size). However, it has been shown that DWI performed in axial and coronal planes yield comparable ADC values [38]. Fourth, we were not able to compare the MRI and histopathology between the right kidneys (in which UUO procedures were performed on) and the contralateral left kidneys. However, the contralateral kidney may not be

considered as the “control” for the right kidney, in which UUO procedure was performed on. In a previous article by Thoeny et al [39], studying IVIM MRI in patients with acute ureteral obstruction, it was shown that MRI parameters were altered (i.e., elevated f) even in the contralateral unobstructed kidneys of patients when compared with the kidneys of normal subjects. In other words, the contralateral unobstructed kidney may be showing a compensatory increase in the glomerular filtration rate due to the obstructed kidney. Therefore, we used the same right kidney, in which only a sham operation was done, and obtained MRI at day 0 as a “control” for kidneys that underwent UUO procedure. Still, we believe that future studies that investigate the role of the contralateral kidney in compensating for the obstructed kidney is needed. Fifth, although we attempted a multiparametric approach consisting of DWI, IVIM MRI and T2*WI and correlated them with multiple histopathological aspects of renal fibrogenesis (changes in cell density and fibrosis area) we did not directly assess “hypoxia”. Such can be done using directly using oxygen electrodes or fiberoptic probes, which is not only invasive but also technically demanding [40]. Other indirect methods include immunohistochemical staining markers such as hypoxia-inducible factor-1 (HIF-1) or vascular endothelial growth factor (VEGF). Future studies showing correlation between MRI and these methods will can be expected to provide further intuition regarding renal fibrogenesis. Sixth, although we looked into two key processes of renal fibrogenesis, increased cell density and increased area of fibrosis (i.e., extracellular matrix deposition), we could not account for the changes in MRI attributed to other factors such as dilatation and atrophy of tubules, increased matrix cross-linking, stiffening of extracellular matrix, and increased oxygen diffusion distance to the tubular cells [2]. Nevertheless, dilatation

of the tubules would, by definition, increase amount of bulk flow or perfusion. Had this been considered into the IVIM modeling, the magnitude of association between D and histopathological findings would have been stronger.

In conclusion, ADC, IVIM MRI-derived parameters, and T2* relaxation time were significantly associated with the area of fibrosis and cell density during renal fibrogenesis in a rabbit model of UUO. The results of our study suggest that multiparametric MRI using the aforementioned sequences have potential for noninvasive assessment modality of renal fibrosis. Further validation in different animal models of renal fibrosis and human clinical studies are needed.

Bibliography

1. Coresh J, Selvin E, Stevens LA, et al. Prevalence of chronic kidney disease in the United States. JAMA. 2007;298:2038-2047.

2. Hewitson TD. Renal tubulointerstitial fibrosis: common but never simple. Am J Physiol Renal Physiol. 2009;296:F1239-1244.

3. Nath KA. Tubulointerstitial changes as a major determinant in the progression of renal damage. Am J Kidney Dis. 1992;20:1-17.

4. Wehrmann M, Bohle A, Bogenschutz O, et al. Long-term prognosis of chronic idiopathic membranous glomerulonephritis. An analysis of 334 cases with particular regard to tubulo-interstitial changes. Clin Nephrol. 1989;31:67-76.

5. Corapi KM, Chen JL, Balk EM, et al. Bleeding complications of native kidney biopsy: a systematic review and meta-analysis. Am J Kidney Dis. 2012;60:62-73.

6. Thoeny HC, De Keyzer F, Oyen RH, et al. Diffusion-weighted MR imaging of kidneys in healthy volunteers and patients with parenchymal diseases: initial experience. Radiology. 2005;235:911-917.

7. Togao O, Doi S, Kuro-o M, et al. Assessment of renal fibrosis with diffusion-weighted MR imaging: study with murine model of unilateral ureteral obstruction. Radiology. 2010;255:772-780.

8. Friedli I, Crowe LA, Berchtold L, et al. New Magnetic Resonance Imaging Index for Renal Fibrosis Assessment: A Comparison between Diffusion-Weighted Imaging and T1 Mapping with Histological Validation. Sci Rep. 2016;6:30088.

9. Chevalier RL, Forbes MS, Thornhill BA. Ureteral obstruction as a model of renal interstitial fibrosis and obstructive nephropathy. Kidney Int. 2009;75:1145-1152.

10. Mahmoud H, Buchanan C, Francis ST, et al. Imaging the kidney using magnetic resonance techniques: structure to function. Curr Opin Nephrol Hypertens. 2016;25:487-493.

11. Le Bihan D, Breton E, Lallemand D, et al. Separation of diffusion and perfusion in intravoxel incoherent motion MR imaging. Radiology. 1988;168:497-505.

12. Koh DM, Collins DJ, Orton MR. Intravoxel incoherent motion in body diffusion-weighted MRI: reality and challenges. Am J Roentgenol. 2011;196:1351-1361.

13. Prasad PV, Edelman RR, Epstein FH. Noninvasive evaluation of intrarenal oxygenation with BOLD MRI. Circulation. 1996;94:3271-3275.

14. Moon SK, Kim SY, Cho JY, et al. Quantification of kidney fibrosis using ultrasonic shear wave elastography: experimental study with a rabbit model. J Ultrasound Med. 2015;34:869-877.

15. Jung SC, Kim SH, Cho JY. A comparison of the use of contrast media with different iodine concentrations for multidetector CT of the kidney. Korean J Radiol 2011;12:714-721

16. Davies B, Morris T. Physiological parameters in laboratory animals and humans. Pharm Res 1993;10:1093-1095

17. Wang Y, Ren K, Liu Y, et al. Application of BOLD MRI and DTI for the evaluation of renal effect related to viscosity of iodinated contrast agent in a rat model. J Magn Reson Imaging. 2017;46:1320-1331.

18. Bauman TM, Nicholson TM, Abler LL, et al. Characterization of fibrillar collagens and extracellular matrix of glandular benign prostatic hyperplasia nodules. PloS One. 2014;9:e109102.

19. Parsons SA, Millay DP, Sargent MA, et al. Age-dependent effect of myostatin blockade on disease severity in a murine model of limb-girdle muscular dystrophy. Am J Pathol. 2006;168:1975-1985.

20. Rosner B. Fundamentals of Biostatistics, Belmont, CA: Duxbury Press. 1995

21. Hennedige T, Koh TS, Hartono S, et al. Intravoxel incoherent imaging of renal fibrosis induced in a murine model of unilateral ureteral obstruction. Magn Reson Imaging. 2015;33:1324-1328.

22. Cai XR, Yu J, Zhou QC, et al. Use of intravoxel incoherent motion MRI to assess renal fibrosis in a rat model of unilateral ureteral obstruction. J Magn Reson Imaging. 2016;44:698-706.

23. Szafer A, Zhong J, Gore JC. Theoretical model for water diffusion in tissues. Magn Reson Med. 1995;33:697-712.

24. Liu Y. Cellular and molecular mechanisms of renal fibrosis. Nat Rev Nephrol. 2011;7:684-696.

25. Woo S, Lee JM, Yoon JH, et al. Intravoxel incoherent motion diffusion-weighted MR imaging of hepatocellular carcinoma: correlation with enhancement degree and histologic grade (Appendix E1). Radiology. 2014;270:758-767.

26. Togao O, Hiwatashi A, Yamashita K, et al. Differentiation of high-grade and low-grade diffuse gliomas by intravoxel incoherent motion MR imaging. Neuro Oncol. 2016;18:132-141.

27. Nangaku M. Chronic hypoxia and tubulointerstitial injury: a final common pathway to end-stage renal failure. J Am Soc Nephrol. 2006;17:17-25.

28. Kang DH, Johnson RJ. Vascular endothelial growth factor: a new player in the

pathogenesis of renal fibrosis. Curr Opin Nephrol Hypertens. 2003;12:43-49.

29. Mao W, Zhou J, Zeng M et al. Intravoxel incoherent motion diffusion-weighted imaging for the assessment of renal fibrosis of chronic kidney disease: A preliminary study. Magn Reson Imaging 2017;47:118-124.

30. Ichikawa S, Motosugi U, Ichikawa T, et al. Intravoxel incoherent motion imaging of the kidney: alterations in diffusion and perfusion in patients with renal dysfunction. Magn Reson Imaging. 2013;31:414-417.

31. Bisdas S. Are we ready to image the incoherent molecular motion in our minds? Neuroradiology. 2013;55:537–540

32. Denis Le Bihan. What can we see with IVIM MRI? Neuroimage. [Epub ahead of print] 2017 Dec 22.

33. Lee S, Lee JM, Yoon JH, Kabasawa H. IVIM with Simultaneous T2 Mapping and Relaxivity Correction. ISMRM 2013 abstract

34. Fine LG, Orphanides C, Norman JT. Progressive renal disease: the chronic hypoxia hypothesis. Kidney Int Suppl. 1998;65:S74-78.

35. Inoue T, Kozawa E, Okada H, et al. Noninvasive evaluation of kidney hypoxia and fibrosis using magnetic resonance imaging. J Am Soc Nephrol. 2011;22:1429-1434.

36. Prasad P, Li LP, Halter S, et al. Evaluation of renal hypoxia in diabetic mice by BOLD MRI. Invest Radiol. 2010;45:819-822.

37. Meng XM, Nikolic-Paterson DJ, Lan HY. Inflammatory processes in renal fibrosis. Nat Rev Nephrol. 2014;10:493-503.

38. Wang HY, Wang J, Tang YH, et al. Coronal diffusion-weighted magnetic resonance imaging of the kidney: agreement with axial diffusion-weighted magnetic imaging in

terms of apparent diffusion coefficient values. Chin Med J. 2015;128:499-503.

39. Thoeny HC, Binser T, Roth B, et al. Noninvasive assessment of acute ureteral obstruction with diffusion-weighted MR imaging: a prospective study. Radiology. 2009;252:721-728.

40. Griffiths JR, Robinson SP. The OxyLite: a fibre-optic oxygen sensor. Br. J. Radiol. 1999;72:627–630.

초 록 (국문)

서론: 본 연구의 목표는 현성확산계수, 복셀 내 화소 결집 운동 확산 자기공명영상 유도 변수들 및 T2* 이완시간과 일측성 요로폐쇄 토끼 동물 모델의 신실질 섬유화 병리학적 변화 간의 관련성을 살펴보고자 하는 것이다.

방법: 본 연구는 본 기관의 동물실험윤리위원회 허가를 받았다 (15-0274-C1A0). 총 20마리의 NZW 토끼 사용하여 일측성 요로 폐쇄 수술을 시행한다. 실험 프로토콜은 각 그룹별 (5마리씩)로 기저 자기공명 영상 촬영 후 수술 (일측성 요로 폐쇄 혹은 가짜 수술), 그리고 술 후 0, 3, 7, 14일 후 추적 자기공명 영상의 스케줄을 따른다. 자기공명영상 촬영은 3-테슬라 장비 (Magnetom Trio, Siemens Medical Solutions, Erlangen, Germany)와 인체용 무릎 코일을 사용하였다. 세포 밀도 분석과 섬유화 면적 (%) 계산을 위해서 헤마톡실린-에오신 및 마손 삼색 염색을 한다. 통계 분석은 일원분산분석, 스피어만 상관 계수, 피어슨 상관계수를 이용한다.

결과: 시간의 흐름에 따라 섬유화 면적과 세포 밀도는 지속적으로 증가하였다: rho = 0.900 (95% 신뢰구간 = 0.760, 0.960; p<0.0001)와 0.904 (95% 신뢰구간 = 0.769, 0.962; p<0.0001). 수술 후 3일 째 모든 MRI 변수들의 신호 강도가 감소하였다가 7일 째에 부분적으로 회복하는 양상을 보였다. ADC, D, f와 T2*

이완시간은 섬유화 면적 및 세포 밀도와 유의한 상관관계를 보였으나 (r = -0.5177과 -0.6962, -0.5395과 -0.7851, -0.7168과 -0.7902, -0.6808과 -0.7212,; p = 0.0052-0.0481) D*는 유의한 상관관계를 보이지 않았다 (p = 0.1997과 0.7853).

결론: 현성확산계수, 복셀 내 화소 결집 운동 확산 자기공명영상 유도 변수들 및 T2* 이완시간은 일측성 요로폐쇄 토끼 동물 모델의 신실질 섬유화 과정 중 섬유화 면적과 세포 밀도의 변화와 유의한 상관성을 보였다. 추가적인 연구들 이후에서 검증될 경우 자기공명영상은 잠재적으로 신실질 섬유화를 비침습적으로 평가할 수 있는 도구가 될 수 있을 것이다.

* 본 논문은 학술지 *Magnetic Resonance imaging* 에 출판 되었음.

Woo S, Cho JY, Kim SY, Kim SH. Intravoxel incoherent motion MRI-derived parameters and T2* relaxation time for noninvasive assessment of renal fibrosis: An experimental study in a rabbit model of unilateral ureter obstruction. Magn Reson Imaging. 2018;51:104-112

주요어: 만성 신질환, 복셀 내 화소 결집 운동 확산, 자기공명 영상, 신실질 섬유화, T2* 강조 영상, 일측성 요로 폐쇄

학번: 2014-30638